Stellarator Turbulence: Subdominant Eigenmodes and Quasilinear Modeling

M.J. Pueschel[1], B.J. Faber[1], J. Citrin[2,3], C.C. Hegna[1], P.W. Terry[1], and D.R. Hatch[4]
[1] *University of Wisconsin-Madison, Madison, Wisconsin 53706, USA*
[2] *FOM Institute DIFFER, 3430 BE Nieuwegein, The Netherlands*
[3] *CEA, IRFM, F-13108 Saint Paul Lez Durance, France*
[4] *Institute for Fusion Studies, University of Texas at Austin, Austin, Texas 78712, USA*

Owing to complex geometry, gyrokinetic simulations in stellarator geometry produce large numbers of subdominant unstable and stable, near-orthogonal eigenmodes. Here, results based on the full eigenmode spectrum in stellarator geometry are presented for the first time. In the nonlinear state of a low-magnetic-shear ion-temperature-gradient-driven case, a multitude of these modes are active and imprint the system. Turbulent frequency spectra are broadband as a consequence, in addition to a nonlinear, narrow signature at electron frequencies. It is shown that successful quasilinear, mixing-length transport modeling is possible in stellarators, where it is essential to account for all subdominant unstable modes.

Heat and particle transport due to turbulence driven by pressure-gradient-driven instabilities constitutes an important limiting factor for fusion reactor performance. One important type of fusion device, the stellarator, is considered a major competitor to tokamaks [1, 2], primarily because it allows for steady-state operation, a feature owing its existence to more complex magnetic geometries. Partly as a consequence of the latter, however, microturbulence and transport in stellarators remain far less understood than in tokamaks. At the same time, complex geometry provides significant flexibility for targeted optimization of stellarators if predictive capabilities can be improved, potentially resulting in greatly enhanced confinement.

One of the challenges of fusion research lies in the intractability of running costly turbulence simulations throughout an enormous physical parameter space, particularly an issue in stellarators. Quasilinear modeling – where heat diffusivities $\chi \sim \gamma/k_\perp^2$ are estimated as the ratio of characteristic growth rates γ to characteristic wave numbers $k_\perp$ – yields approximate answers at orders of magnitude lower cost and can be used as a basis for training ultra-fast emulators [3], making for an excellent tool to optimize reactor operation and control. In many cases, however, quasilinear physics are investigated taking into account only the most unstable eigenmode in the system, while in complex stellarator geometries, many such instabilities tend to exist concurrently. As will be shown in this work, an appropriate reduced model must take all such modes into account.

Subdominant – meaning of growth rate $0 < \gamma < \gamma_{\max}$ – and stable modes in plasma microturbulence have received attention in the context of anomalous transport in tokamaks, both for the capacity of individual such modes to contribute to the turbulent state [4–6] and the collective role of stable modes in energy dissipation and saturation [7–9]. Where stellarators are concerned, little is known about such modes, aside from the existence of subdominant modes in experimentally relevant scenarios [10, 11]. Such considerations are of great importance to confinement in fusion devices: turbulent excitation of subdominant and stable modes may, through various means, affect structure formation as well as heat and particle transport. In this work, important aspects of subdominant and stable mode activity in stellarators are elucidated: their turbulent excitation, their mode structure and orthogonality, their imprint on the nonlinear frequencies, and their role in causing transport and effect on quasilinear modeling.

In fusion plasmas, microturbulence commonly contributes significantly to the overall heat and particle transport. In such scenarios, temperature and density gradients drive instabilities at scales somewhat larger than the gyroradius, which in turn causes turbulence and transport. Gyrokinetics [12] provides an extensively used framework for investigating such processes, reducing the six-dimensional kinetic phase space through the elimination of the gyrophase and its associated fast gyrofrequency. Gyrokinetics has been applied [13] to stellarators mostly in the radially local limit, where flux tube shapes depend on the toroidal position in the device, an approach adopted here, as well. Extending the present work to full-flux-surface computations is left to future investigations. See Ref. [14] for details on the implementation of gyrokinetics in the GENE code [15, 16], which will be used throughout this paper.

Figure 1 shows the linear eigenvalue spectrum at the wavenumber $k_y = 0.7$ – the nonlinear transport peak – for profile parameters $\omega_{T\mathrm{i}} \equiv a(\nabla T_{\mathrm{i}0})/T_{\mathrm{i}0} = 3$ and $\omega_n \equiv a(\nabla n_{\mathrm{e}0})/n_{\mathrm{e}0} = 1$, with magnetic shear $\hat{s} = -0.045$ and adiabatic electrons. All unstable modes are ion-temperature-gradient-driven modes, their number – 66 for the default case – far exceeding typical numbers in tokamak core plasmas [17]. The magnetic geometry is identical to that of the HSX "bean" flux tube in Ref. [11], although flux tube choice does not significantly affect results. Note that these parameters were not chosen to reflect a specific experimental scenario. a denotes the minor radius, $T_{\mathrm{i}0} = T_{\mathrm{e}0}$ and $n_{\mathrm{e}0}$ the background ion temperature and electron density, and wavenumbers are nor-

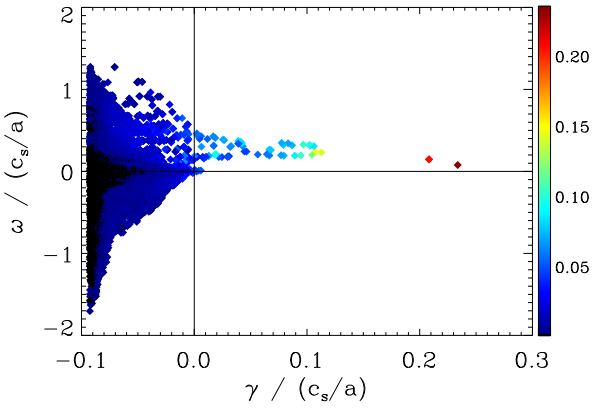

FIG. 1. (Color online) Linear eigenmodes by growth rate γ and frequency ω. Colors denote nonlinear excitation p, see the text, in the quasi-stationary state. A total of 10^4 eigenvalues are shown here, 66 of which are linearly unstable. Note: the point at $\gamma \approx 0.2$ consists of two distinct modes, see Figs. 3,4.

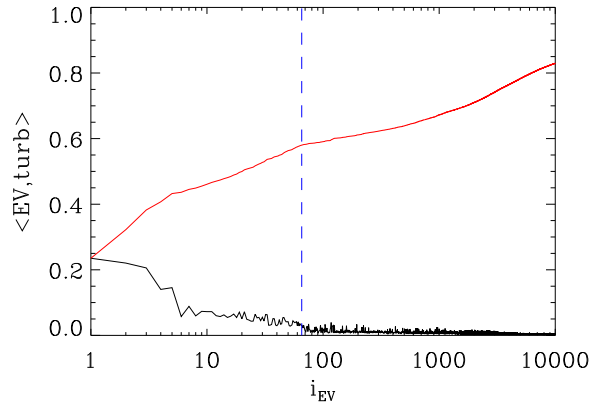

FIG. 2. (Color online) Projection p (black; see the text) for orthogonalized eigenmodes; nonorthogonal modes are unstable up to $i_{\rm EV} = 66$ (blue dashed line). The upper, red curve shows the square root of the sum, truncated at $i_{\rm EV}$, of p^2, a measure of how well a given truncation cumulatively describes the nonlinear state.

malized to the inverse ion sound gyroradius $\rho_{\rm s}$. This case can be resolved by as few as 9 radial modes and 72 parallel grid points, for a total of 165888 eigenvalues. See Ref. [11] for a discussion of the simulation domain—similar settings allow converged simulations in the present case. For the default case, the full spectrum was computed, whereas for the quasilinear study, GENE's iterative solver obtained up to 200 modes per k_y and $\omega_{T\rm i}$.

Color-coded in Fig. 1, the excitation p of each eigenvector g_i in the nonlinear state $g_{\rm NL}$ is given by the time average of the projection

$$p = \left| \int \mathrm{d}\mathbf{x}\mathrm{d}\mathbf{v}\, g_i^* g_{\rm NL} \right| \left(\int \mathrm{d}\mathbf{x}\mathrm{d}\mathbf{v}\, |g_i|^2 \int \mathrm{d}\mathbf{x}\mathrm{d}\mathbf{v}\, |g_{\rm NL}|^2 \right)^{-1/2}, \quad (1)$$

which ranges from 0 (orthogonal g_i and $g_{\rm NL}$) to 1 (when $g_i \propto g_{\rm NL}$). The most unstable mode only has $p \lesssim 0.25$, due to a large number of subdominant and stable modes contributing to the nonlinear state, whereas data [17] for a typical tokamak case yields $p \gtrsim 0.7$. Importantly, both cases exhibit fairly orthogonal eigenmode spectra, with the stellarator being even more orthogonal: the scalar product, defined equivalently to p, of the most unstable with 199 subdominant and stable modes, exceeds 0.2 for only two modes, compared with 22 in the tokamak. Intuitively, this is explained by invoking the large number of regions in ballooning space where unstable or weakly stable modes may peak, a consequence both of the complex parallel geometry and small magnetic shear.

While it is possible to use the direct eigenvalue decomposition for almost all analyses, Fig. 2 shows the cumulative composition of the nonlinear state by eigenmode truncation for orthogonalized data: All unstable modes combined are only able to describe slightly more than half of the nonlinear features of the system, compared with more than 70% for the first mode alone in the tokamak,

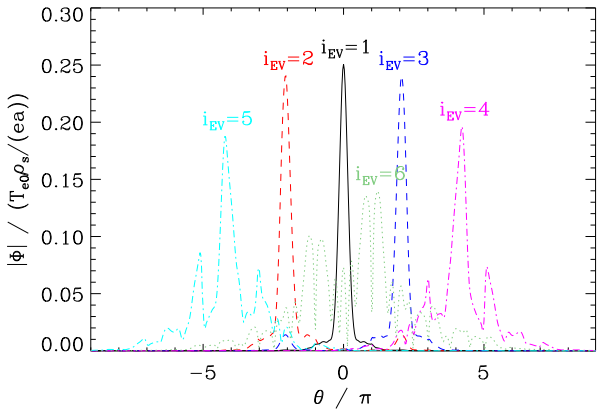

FIG. 3. (Color online) Eigenmode structure in the electrostatic potential as a function of extended ballooning angle, for the six most unstable modes: $i_{\rm EV} = 1$ (solid black), 2 and 3 (dashed red and blue), 4 and 5 (dash-dotted pink and cyan), and 6 (dotted green).

assigning significantly more importance to the physics of stable modes. Furthermore, there exist two visible breaks in the cumulative projection: one at $i_{\rm EV} \approx 5$ – related to the mode structures discussed next – and one at the transition between unstable and stable modes at $i_{\rm EV} = 66$.

Examining the eigenmode structure of the six most unstable modes, see Fig. 3, one observes that the low-field side is preferred, where the ballooning angle θ is an integer multiple of 2π. Modes peaking at radial wavenumbers $k_x \neq 0$ (where $|\theta| > \pi$) occur in symmetric pairs of near-identical eigenvalues. The sixth mode is representative of many of the higher-$i_{\rm EV}$ modes, where more complex structures appear and unique mode identification becomes very difficult.

This last property is evident in Fig. 4, where eigenvalue

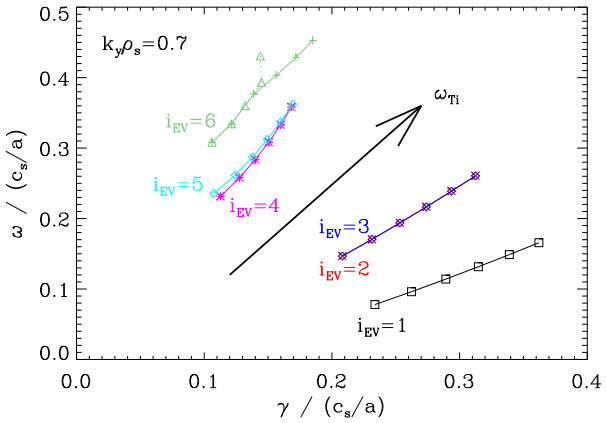

FIG. 4. (Color online) Effect of the driving gradient $\omega_{T\mathrm{i}}$ on the first six eigenvalues (same colors as in Fig. 3), with $\omega_{T\mathrm{i}}$ increasing left-to-right from 3 in steps of 0.3. For $i_{\mathrm{EV}} = 6$, mode identification becomes difficult at higher $\omega_{T\mathrm{i}}$, and plus signs/triangles denote two possible paths.

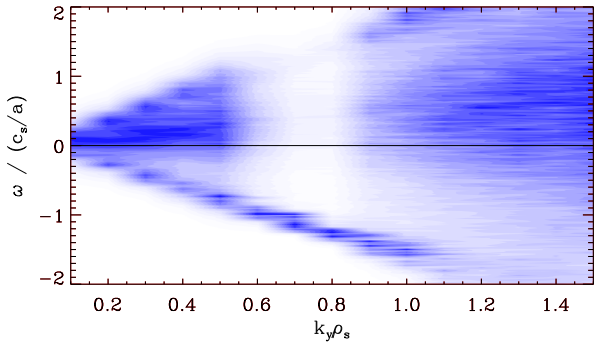

FIG. 5. (Color online) Nonlinear frequencies as a function of wavenumber. Colors indicate intensity, normalized separately for every k_y. The broad band at positive ω corresponds directly to the linear frequencies of the unstable modes, with an additional narrow band of negative (electron-direction) frequencies of nonlinear nature.

dependence on the driving gradient is shown. The most unstable modes are easily identified, exhibiting growth rates and frequencies mostly proportional to $\omega_{T\mathrm{i}}$. Again, $i_{\mathrm{EV}} = 6$ is representative of higher mode numbers, in that at this point, identification is no longer possible, and small changes in input parameters will result in rather different eigenvalue order. While a caveat for automated analyses based on i_{EV}, this issue becomes less prominent when summing over large numbers of modes. These properties, however, also illustrate that linear critical gradients would have to be computed separately for all modes, and may not exist in all cases.

Extracting frequency signatures from nonlinear simulations and comparing with linear mode frequencies is a valuable tool in identifying eigenmode activity in the nonlinear state. While in many cases, linear frequencies match nonlinear spectra [5], recent work in HSX geometry demonstrated that nonlinear frequencies in trapped electron mode turbulence may deviate strongly [11]: in addition to electron-direction frequencies much lower than linear predictions, the nonlinear data included a strong and narrow ion-direction band of frequencies proportional to k_y. This latter feature could not be explained by the behavior of linear eigenmodes.

In the present case, while solving for the full linear eigenmode spectrum is rather expensive, nonlinear simulations are much cheaper (although still much more expensive than solving for a small subset of linear modes), resulting in statistically very accurate transport and frequency data. The latter is shown in Fig. 5, where nonlinear frequencies are plotted as a function of k_y. The wide range of linear frequencies of the unstable modes – ranging from zero to approximately 0.5 – is visible in the positive range of nonlinear frequencies. The broad-band structure of the latter is a direct consequence of the large number of subdominant linear eigenmodes, and the peak of the (positive) nonlinear data agrees with the most unstable linear modes. However, a narrow band of negative frequencies proportional to k_y is also apparent. These frequencies are not affected by changes in ω_n or $\omega_{\mathrm{T}i}$, and thus cannot be attributed to electron drift waves—an effort is underway to determine its nonlinear origins. While cases exist where nonlinear features affect transport [11], no indication is given that the nonlinear frequency feature in the present simulations has a measurable effect in that regard.

Turning to turbulent heat transport, quasilinear models – where nonlinear transport is estimated from linear mode properties and characteristic length scales [18] – are investigated next. To account for stellarator geometry [19, 20], one needs to use a generalized expression for the heat diffusivity (using GENE normalization):

$$\chi_{\mathrm{i}}^{\mathrm{QL}} = \mathcal{C} \sum_{k,i} S_k \frac{w_{k,i}\gamma_{k,i}}{\langle k_{\perp k,i}^2 \rangle} \ , \tag{2}$$

with

$$\langle k_\perp^2 \rangle = \left\langle \frac{k_y^2 \left[1 + (g^{xy} + \hat{s}\theta_0(k_x) g^{xx})^2\right]}{g^{xx}} \right\rangle \ . \tag{3}$$

Here, $\mathcal{C}$ is a scalar and model constant. Respectively, sums over indices k and i are over k_y wavenumbers and unstable eigenmodes. The shape of the nonlinear flux spectrum is described by the k_y-dependent factor S_k, while $w = Q_{\mathrm{i}}/n^2$, heat flux divided by squared density, is the quasilinear weight of a given mode. $\theta_0(k_x) = 0, \pm 2\pi, \ldots$ is the extended ballooning angle at the low-field side for a given k_x. The quantities Λ and $|\nabla\Psi|^2$ in Ref. [19] become – omitting normalization factors – the metric coefficients g^{xy} and g^{xx}, respectively. For the average $\langle \ldots \rangle$, the electrostatic potential Φ of a given eigen-

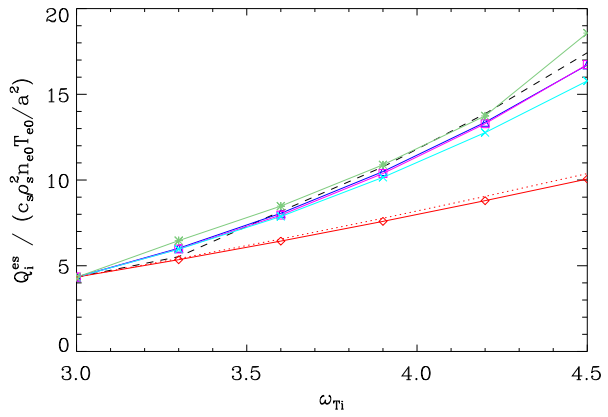

FIG. 6. (Color online) Transport predictions from quasilinear models as a function of driving gradient. Model 1: red diamonds, 2: blue triangles, 3: pink squares, 4: cyan crosses, 5: green stars. The actual transport from a nonlinear scan is shown as a black dashed line, and is only recovered by models that include all unstable modes. For reference, a dotted red line denotes model 1 when the 5 most unstable modes are included, exhibiting little difference from only the most unstable mode.

mode is used as a weight:

$$\langle A \rangle \equiv \frac{\int \mathrm{d}\theta A |\Phi|^2}{\int \mathrm{d}\theta |\Phi|^2} \ . \tag{4}$$

With these definitions, the following quasilinear models are constructed, most of which are reduced versions of Eq. (2), increasing in complexity: 1. accounting for only the most unstable mode, $\chi_\mathrm{i}^\mathrm{QL} \propto \max_i \gamma_i$; 2. retaining all unstable modes, $\sum_i \gamma_i$; 3. additionally taking into account the term $\sum_i (\gamma_i / \langle k_\perp^2 \rangle)$; and 4. furthermore including the quasilinear weights w. The separation of terms in these models is not to suggest that such simplified models are universally applicable, but is rather meant to measure contributions from different terms.

Models 1 through 4 use shapes S_k that merely match the nonlinear data from a reference simulation. An additional model 5, based on the more general saturation rule of the QuaLiKiz code [21], models the shape of the flux spectrum by power laws and is otherwise identical to model 4. It estimates the peak of the nonlinear flux spectrum from the maximum of $w\gamma/\langle k_\perp^2 \rangle$, then fitting distinct power laws for larger and smaller k_y. Possible further improvement of this model would involve interpolating this maximum between discrete k_y.

Quasilinear heat diffusivities are multiplied by $\omega_{T\mathrm{i}}$ to arrive at heat fluxes Q_i, and $\mathcal{C}$ is determined from the base nonlinear run at $\omega_{T\mathrm{i}} = 3$. As shown in Fig. 6, model 1 predicts far too small an increase of Q_i with $\omega_{T\mathrm{i}}$, and even when including the five most unstable modes, little improvement is seen. All refinements applied after model 2 – the inclusion of $k_\perp$ corrections and transport weights – have little impact on the predictions; for $k_\perp$, this is a consequence of the low magnetic shear in HSX geometry, and cannot be expected to hold true in higher-shear configurations. Note also that model 5 is somewhat more successful than other models at capturing the precise shape of the k_y-resolved transport as $\omega_{T\mathrm{i}}$ is increased.

As zonal flows are known to regulate transport, it is helpful to study the scaling of the shearing rate $\omega_\mathrm{s} = \langle k_x^2 \Phi_\mathrm{zonal} \rangle_{x,t}$ relative to the linear growth rate [10, 22–25], where Φ_zonal is the flux-surface-averaged potential. For the present case, the shearing rate increases at constant increment from 0.32 to 0.57, somewhat less steeply than the peak γ. This is consistent with increasing/decreasing transport in zonal-flow-regulated turbulence being related to increasing/decreasing γ/ω_s, respectively—a prerequisite for quasilinear modeling to apply.

In summary, the excitation, behavior, and impact of subdominant and stable eigenmodes in stellarator turbulence have been investigated. Unlike in tokamaks, the turbulent energy is split more evenly between a large number of eigenmodes. Nonlinear frequency analysis shows a correspondingly broad range of excitation of linear frequencies, in addition to a nonlinear narrow-band structure at opposite sign, an object of future study. It remains to be ascertained whether such features are a common occurrence in stellarator microturbulence [11].

More generally, the present results indicate that in order to employ linear physics to predict transport behavior in stellarators – as is done in stellarator optimization, where quasilinear or linear models are often employed as proxies [26, 27] – one is required to take the full unstable eigenmode spectrum into account.

While these findings show that a significant increase in computational effort is required to solve for all unstable modes when computing quasilinear fluxes in stellarators, they also confirm for the first time that for this class of machines, quasilinear modeling yields good transport predictions. Not as efficient as for tokamaks, it nonetheless requires only a tiny fraction – on the order of a percent – of the nonlinear simulation cost. Future investigations will need to confirm whether these results apply to kinetic-electron or full-flux-surface simulations, where other important physics come into play.

The authors thank D. Told for helpful discussions. Support was received through U.S. DOE grants *DE-SC0006103* and *DE-FG02-99ER54546*. Computing time was provided through the National Energy Research Scientific Computing Center, a DOE Office of Science User Facility, grant *DE-AC02-05CH11231*.

[1] K. Kiyamoto, Nucl. Fusion **18**, 243 (1978)
[2] P. Helander, Rep. Prog. Phys. **77**, 087001 (2014)
[3] J. Citrin *et al.*, Nucl. Fusion **55**, 092001 (2015)
[4] M.J. Pueschel, M. Kammerer, and F. Jenko, Phys. Plasmas **15**, 102310 (2008)

[5] F. Merz and F. Jenko, Nucl. Fusion **50**, 054005 (2010)
[6] D.R. Hatch *et al.*, Phys. Rev. Lett. **108**, 235002 (2012)
[7] D.R. Hatch *et al.*, Phys. Plasmas **18**, 055706 (2011)
[8] K.D. Makwana, P.W. Terry, M.J. Pueschel, and D.R. Hatch, Phys. Rev. Lett. **112**, 095002 (2014)
[9] P.W. Terry *et al.*, Phys. Plasmas **21**, 122303 (2014)
[10] P. Xanthopoulos, F. Merz, T. Görler, and F. Jenko, Phys. Rev. Lett. **99**, 035002 (2007)
[11] B.J. Faber *et al.*, Phys. Plasmas **22**, 072305 (2015)
[12] A.J. Brizard and T.S. Hahm, Rev. Mod. Phys. **79**, 421 (2007)
[13] P. Helander *et al.*, Nucl. Fusion **55**, 053030 (2015)
[14] P. Xanthopoulos and F. Jenko, Phys. Plasmas **13**, 092301 (2006)
[15] F. Jenko, W. Dorland, M. Kotschenreuther, and B.N. Rogers, Phys. Plasmas **7**, 1904 (2000)
[16] see `http://www.genecode.org` for code details and access
[17] M.J. Pueschel *et al.*, Phys. Plasmas **20**, 102308 (2013)
[18] F. Jenko, T. Dannert, and C. Angioni, Plasma Phys. Control. Fusion **47**, B195 (2005)
[19] C.C. Hegna, Phys. Plasmas **7**, 3921 (2000)
[20] P. Xanthopoulos *et al.*, Phys. Plasmas **16**, 082303 (2009)
[21] C. Bourdelle *et al.*, Phys. Plasmas **14**, 112501 (2007)
[22] R.E. Waltz, G.D. Kerbel, and J. Milovich, Phys. Plasmas **1**, 2229 (1994)
[23] T.S. Hahm *et al.*, Phys. Plasmas **6**, 922 (1999)
[24] P.H. Diamond, S.-I. Itoh, K. Itoh, and T.S. Hahm, Plasma Phys. Control. Fusion **47**, R35 (2005)
[25] M.J. Pueschel and F. Jenko, Phys. Plasmas **17**, 062307 (2010)
[26] H. Mynick *et al.*, Plasma Phys. Control. Fusion **56**, 094001 (2014)
[27] J.H.E. Proll, H.E. Mynick, P. Xanthopoulos, S.A. Lazerson, and B.J. Faber, Plasma Phys. Control. Fusion **58**, 014006 (2015)